Design of a 1-THz 4th-Harmonic Gyrotron Driven by Large-orbit beam

Fan-Hong Li, Chao-Hai Du, Senior Member, IEEE, Zi-Wen Zhang, Si-Qi Li, Zi-Chao Gao, Pu-Kun Liu, Guo-Wu Ma, Qi-Li Huang, Hong-Ge Ma, Liang Zhang, Senior Member, IEEE, and Adrian W. Cross, Member, IEEE

Abstract— In this paper, the design of a 4th-harmonic gyrotron with 1-kW-level output power at 1 terahertz (THz) is presented. A unique advantage of this design is that, with a well-optimized magnetic-cusp large-orbit electron gun, the designed gyrotron can operate from 1st harmonic to 4th harmonic in multiple discrete bands by varying the operating voltage. By carefully balancing the competing modes, the gyrotron can be tuned to operate at six candidate modes, including $TE_{1,2}$ for fundamental harmonic, $TE_{2,3}$ and $TE_{2,4}$ for 2nd harmonic, $TE_{3,5}$ and $TE_{3,6}$ for 3rd harmonic, and $TE_{4,8}$ for 4th harmonic interactions. As the main operating mode, the $TE_{4,8}$ can generate a peak output power of 1.68 kW, with an efficiency of about 2.1%, and a magnetically controlled frequency tuning range of about 1.8 GHz around 1 THz. The impact of the longitudinal nonuniformity of the cavity at high-harmonic interaction was also studied. It shows a radial tolerance of several micrometers will significantly elevate the start-oscillation current and deteriorate output performance. This design is towards the development of a synthesizing THz source with ultra-wideband tuning capability ranging from the sub-millimeter-wave to 1-THz bands.

Index Terms—high harmonic terahertz gyrotron, multi-mode switching, broad-range magnetic tuning.

I. INTRODUCTION

Recent developments of terahertz (THz) technologies have put great demands on high-performance THz sources [1], such as the dynamic nuclear polarization enhanced nuclear magnetic resonance (DNP-NMR) spectroscopy [2], and the extreme ultraviolet (EUV) lithography [3]. In these applications, high power and high-frequency continuous-wave CW sources are desired. Gyrotrons based on the electron cyclotron maser are one of the promising sources for generating coherent electromagnetic (EM) radiation, which has undergone a significant advancement towards the THz band [4], [5], [6]. The radiation frequency of a gyrotron can be approximated as the harmonic cycling frequency of electron beams

$$\omega \approx seB_0 / \gamma m_0 \qquad (1)$$

where ω is the radiation angular frequency, s is the harmonic number, e is the electron charge, B_0 is the field strength of the external magnet, γ is the relativistic factor, and m_0 is the electron rest mass. According to (1), a high-field magnet of about 40 T is required for fundamental harmonic ($s = 1$) operation at 1 THz. The generation of such a high magnetic field at the CW regime is impossible using the contemporary superconducting magnet, therefore, a higher- harmonic ($s > 1$) gyrotron is more attractive since the required magnetic field strength can be greatly reduced compared with fundamental harmonic.

Terahertz and sub-terahertz harmonic gyrotrons have been extensively explored in the past decades [7]. The report on sub-terahertz 2nd harmonic gyrotrons can be found in the early 1970s [8]. A 326-GHz (CW) gyrotron was designed and tested at the Institution of Applied Physics (IAP), the Russian Academy of Sciences (RAS) [8]. It operated at the 2nd harmonic with an output power of 1.5 kW and an efficiency of 6.2%. Again at IAP, RAS, the 526 GHz and 1.288 THz gyrotrons were designed and experimentally tested [9], [10]. At Massachusetts Institute of Technology (MIT), USA, a multi-mode gyrotron was designed and experimentally tested, where 14 different 2nd harmonic TE modes were employed to generate radiation at the frequency range of 301 - 503 GHz and the output powers range in 1-22 kW [11]. At the University of Electronic Science and Technology of China (UESTC), China, gyrotrons employing various 2nd harmonic TE modes were designed and experimentally verified from 395 GHz to 679 GHz [12],[13], [14], [15], At the University of Fukui (FU), Japan, two main series of gyrotron were developed, i.e., the FU series and the FU CW series [16]. The FU CW III gyrotron operated at the 2nd harmonic with a frequency exceeding 1 THz [17], [18].

There remain challenges in the development of high frequency and harmonic gyrotrons, such as mode competition, ohmic loss, misalignment, etc.

Using axis-encircling electron beams, also called large orbit beams (LOB), could be an effective method to suppress the mode competition. Harmonic gyrotrons (especially $s > 3$) based on LOBs have been widely investigated in the past decades. The 1-THz large orbit gyrotron (LOG) operated at 3rd harmonic was developed and tested in IAP, RAS [19]. A LOG which can operate at the 5th harmonic with a permanent magnet

was constructed and experimentally investigated at FU, Japan [20].In this paper, a cusp electron gun generating LOBs was employed for the design and development of the 1-THz 4th harmonic gyrotron. The design process and the optimized parameters of the electron gun are detailed in [21].

This paper presents the design of the multi-mode gyrotron currently under development. The main operating mode is the 4th harmonic $TE_{4,8}$ mode at 1 THz. In Section II, the parameters of the interaction circuit and configuration of the electron optics system are presented. The ohmic loss model including the surface roughness in frequency- and time-domain theory is briefly described. The influence of the nonuniformity of the interaction circuit on start-oscillation current is investigated. In section III, the output characteristics of the gyrotron are calculated and shown. To investigate the gyrotron operating at a wide range of magnetic field strengths, the simulated LOB parameters of the employed cusp electron gun at the corresponding various magnetic field strengths are used in the calculation. The output characteristics of the $TE_{4,8}$ mode at various currents, voltage, and magnetic field strengths are demonstrated. The output characteristic and tuning strategy in multi-mode switching are demonstrated at the end of Section III. To adopt the misalignment correction strategy, the gyrotron can be operated in modes of various lower harmonics. A misalignment correction strategy is discussed in Section IV. The conclusion is drawn in Section V.

II. DESIGN AND MODELING OF THE GYROTRON

A. Geometry Structure and Magnet Configuration

The interaction cavity consists of three sections, i.e., the cut-off, the uniform, and the output-taper sections. The interaction structure is shown in Fig. 1. The geometry parameters are detailed in Table I. The operating mode is $TE_{4,8}$, whose cut-off frequency of the uniform section is 1 THz. Correspondingly, the radius of the uniform section, R_2, is 1.373 mm. The length of the uniform section is close to 30λ, where λ is the wavelength in vacuum at the operating frequency. The radius of the left-hand side of the cut-off section, R_1, is equal to $0.8 R_2$. The length of the cut-off section, L_1 is close to 10λ. The oblique angle of the output taper is 1.57°. The output taper in the practical gyrotron is much longer than L_3. It is truncated in the simulation to reduce the computing time, however without changing the output performance. The magnet configuration and the entire structure of the output taper are shown in Fig. 2. The 3-D model of the engineering design for the hot test is shown in Fig. 3.

Table I Geometry Parameters of the Interaction Circuit

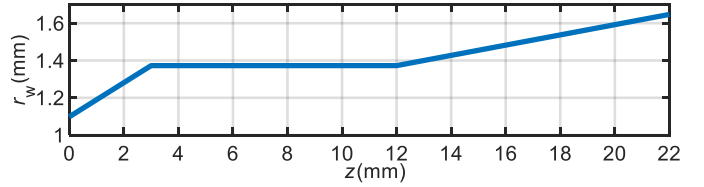| Parameters	Values (mm)
R_1	1.098
R_2	1.373
R_3	1.647
L_1	3.00
L_2	9.00
L_3	10.00

Fig. 1. Longitudinal structure of the interaction circuit. It is a three-segment structure.
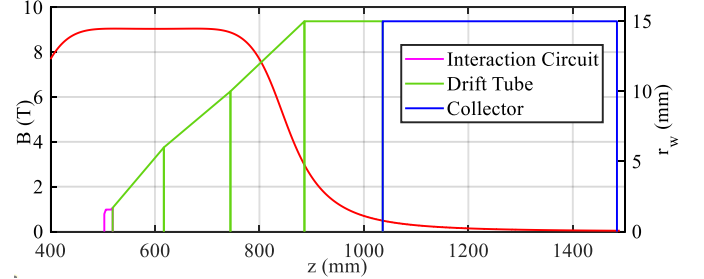

Fig. 2. Geometry structure of the interaction circuit (pink), the drift tube (green), and the collector (blue). The red line is the longitudinal profile of the external magnetic field.
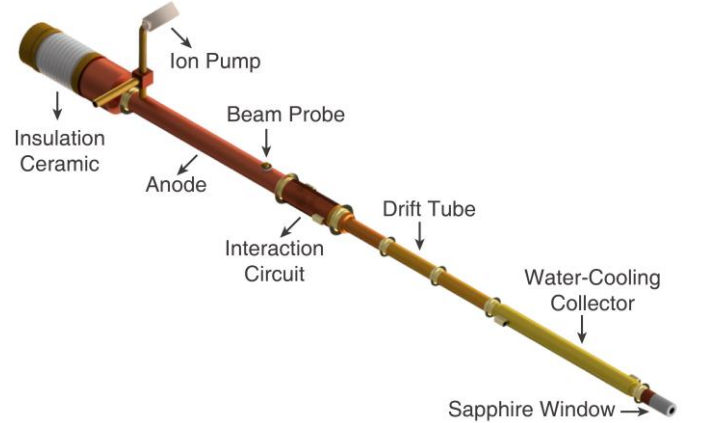

Fig. 3. The 3-D design model of the 1-THz gyrotron tube.

B. Electron Beams

TABLE II. BEAN PARAMETERS OF THE MCG

Parameters	Symbol	Value
Pitch Factor	α	1.50
Main Magnetic Field	B_0	10.3 T
Emission Current	I	1 A
Acceleration Voltage	U	80 kV
Larmor Radius	r_L	78.94 μm
Guiding Center Radius	r_g	28.77 μm
Transverse Velocity Spread	δv_t	10.13%
Axial Velocity Spread	δv_z	22.71%

A magnetic cusp gun (MCG) is employed to partly suppress the parasitic modes [21]. The electron gun can operate in a wide range by tuning the auxiliary coil. In [21] only the results in 8.0-10.0 T were presented, however the electron gun can generate desired electron beams in 7.0-10.5 T. The parameters of the electron beams generated by the MCG at 10.3 T are detailed in Tab. II. The designed transverse velocity spread caused by the electron optical system is about 4.07%. With the consideration of factors like roughness and thermal effects in the emitter surface [22], the transverse velocity spread is 10.13%. Based on the relationship between the transverse and axial velocity spread [23], [24], [25], the axial velocity spread used in the simulations is 22.71%.
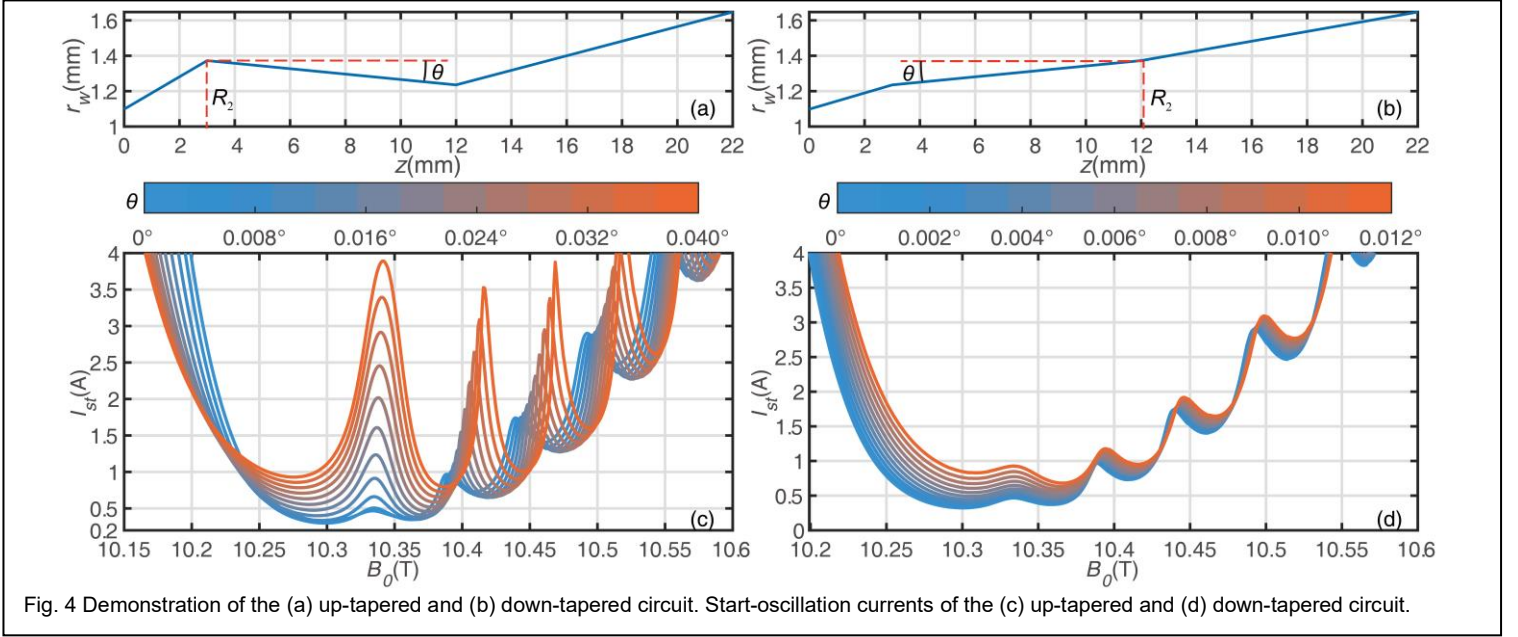
Fig. 4 Demonstration of the (a) up-tapered and (b) down-tapered circuit. Start-oscillation currents of the (c) up-tapered and (d) down-tapered circuit.

C. The Operating Modes and Competition Modes.

The operating mode is the $TE_{4,8}$ mode. The beam-wave coupling factor is expressed as [4]

$$H_{sm} = J_{s-m}^2 \left(k_{mn} r_g \right) J_s'^2 \left(k_{mn} r_L \right) \qquad (2)$$

where J is the Bessel Function of the first kind, k_{mn} is the cut-off wavenumber for the $TE_{m,n}$ mode. The beam-wave coupling strength diagram is shown in Fig. 5. Except for the 4th-harmonic modes and 5th-harmonic modes, there remain 5 modes as the competition modes, i.e., $TE_{1,2}$ of the fundamental harmonics, $TE_{2,3}$ and $TE_{2,4}$ of the second harmonics, and $TE_{3,4}$, $TE_{3,5}$, and $TE_{3,6}$ of the third harmonics. The abscissa values of the stems in Fig. 5 are equal to x_{mn}/s, where x_{mn} and s are the eigenvalues and the harmonic indices of related modes, respectively.
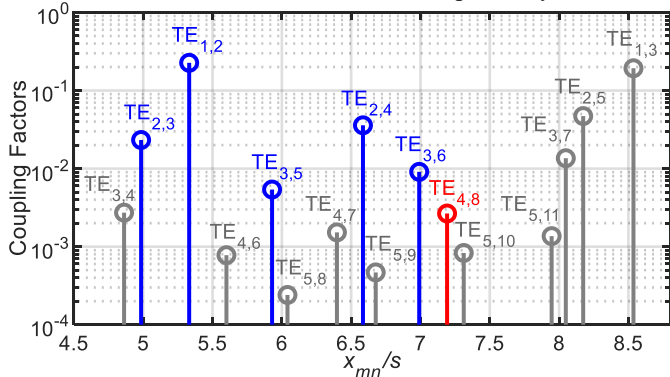

Fig. 5 Coupling factors of the main operation mode $TE_{4,8}$ (red) and its neighbour modes (blue).

D. Model for Surface Roughness

The skin depth decreases when the operating frequency elevates. Excess loss due to surface roughness occurs when the surface roughness is on the relatively same scale as the skin depth of the metal material [26]. Hammerstad-Bekkadal (HB) formula [27] is used to evaluate the Ohmic loss due to surface roughness. The effective conductivity of the metallic wall σ_{eff} is evaluated as

$$\sigma_{eff} = \sigma_0 \cdot \left\{ 1 + \frac{2}{\pi} \arctan \left[1.4 \left(\frac{h}{\delta} \right)^2 \right] \right\}^{-2} \qquad (3)$$

where h is the RMS height of the surface, δ is the skin depth, and σ_0 is the conductivity for a flat and smooth surface. In this paper, $\sigma_0 = 5.8 \times 10^7$ S/m, $h = 896$ nm (35.2 μin) was used. In this case σ_{eff} equals 1.45×10^7 S/m (~$0.25\sigma_0$). By substituting the evaluation of H-B formula into the impedance wall, it is convenient to combine the surface roughness with the analytical models including the steady-state frequency-domain theory [28], [29], [30] and the multimode time-domain theory [31], [32].

E. Nonuniformity of the Interaction Circuit

Based on the single-mode frequency-domain theory [28], [29], [30], the start-oscillation currents (I_{st}) of $TE_{4,8}$ and the parasitic modes are plotted in Fig. 4. It should be noted that instead of sharing the same beam parameters for the six modes, each mode adopts the beam parameters corresponding to its own operating magnetic field [33]. The beam parameters at various magnetic field strengths are extracted from the electron gun simulations, which are partly presented in [21]. When turning the inner wall of cylindrical waveguides, the abrasion wear of cutting tools tends to influence the longitudinal uniformity of the waveguide. The non-uniformity can be divided into two cases by the machining directions of the cutting tool, i.e., the up- and down-tapered cases. The two cases are shown in Fig. 4 (a) and (b) for comparison. The value of L_2 keeps constant at various oblique angles. For the up-tapered case, the turning process starts from the cathode end with the initial radius R_2, while for the down-tapered case, the turning starts from the collector end. The start-oscillation currents of the two cases are shown in Fig. 4 (c) and (d). For the up- and down-tapered circuits, the influences on the I_{st}s are different. In up-tapered cases, the minimum I_{st}s for the first axial mode exceed 1 A
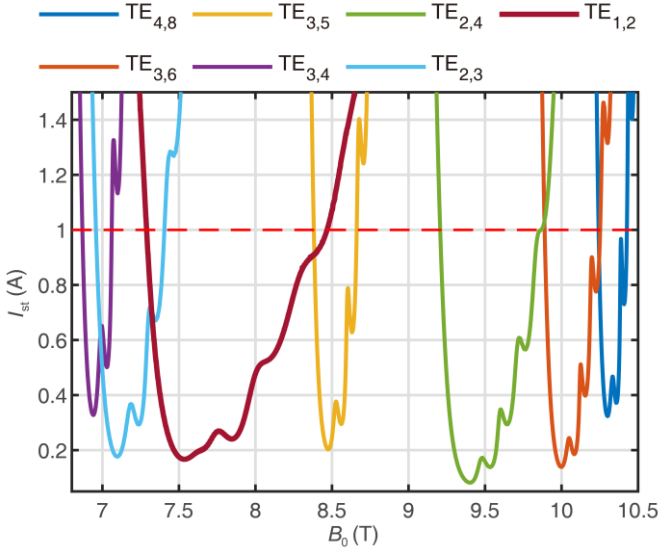
3

Fig. 6 Start-oscillation currents of the main operating mode and other parasitic modes.

when the oblique angle is 0.012° (1.9 μm difference in radius), while in the down-tapered cases it is 0.040° (6.3 μm). Therefore, the down-tapered circuit will have a more severe influence on the beam-wave interaction than the up-tapered circuits. In up-tapered cases, the I_{st}s decrease first and then increase, while it only elevated for down-tapered cases. Hence, it is better to turn from the cathode-end of the circuit when considering the abrasion wear of the cutting tool. Besides, employing other fabrication approaches, such as wire cutting could be a better option for good uniformity, however the surface roughness may be worse.

III. MULTI-MODE SELF-CONSISTENT CALCULATION

A. Output Performance of TE$_{4,8}$

The time-domain calculation is carried out taking into account the TE$_{4,8}$ mode and the most dangerous competing mode TE$_{3,6}$ mode. At 10.3 T, both the TE$_{4,8}$ mode and the TE$_{3,6}$ mode can be excited. The TE$_{3,6}$ has a shorter start-oscillation time than the TE$_{4,8}$, which means that TE$_{3,6}$ mode will start oscillation first. After that, the TE$_{3,6}$ mode will be suppressed by the next start-oscillation mode TE$_{4,8}$. Finally, the TE$_{4,8}$ mode enters the stationary oscillation status after tens of nanoseconds. In stationary oscillation status, the output power normally keeps steady unless the mode operates at the non-stationary oscillation region [34]. The output performances at various voltages and currents are shown in Fig. 7. In current tuning, the TE$_{4,8}$ mode is excited at 10.3 T under a beam current of 1 A. The current keeps constant until the TE$_{4,8}$ enters the stationary status, and then the beam current is reduced. In the current tuning mode, the TE$_{4,8}$ mode can operate at the hard-self-excitation point. In other words, the TE$_{4,8}$ mode keeps oscillating, although the operating current is lower than the I_{st} (0.33 A) of the TE$_{4,8}$ mode. The ohmic loss power is about four times higher than the output power.

In voltage tuning shown in Fig. 8, the output and ohmic loss power curves are the syntheses of power curves in 70 – 80 kV and 80 – 90 kV. In two voltage tuning ranges, the TE$_{4,8}$ mode is excited at 10.3 T and 80 kV, the beam voltage keeps unchanged until the TE$_{4,8}$ starts oscillating steadily. The

maximum output power locates near 82.7 kV. The output characteristics as the function of magnetic field strengthsare shown in Fig. 8. The output and ohmic loss power curves are the syntheses of power curves in 10.25 – 10.3 T and
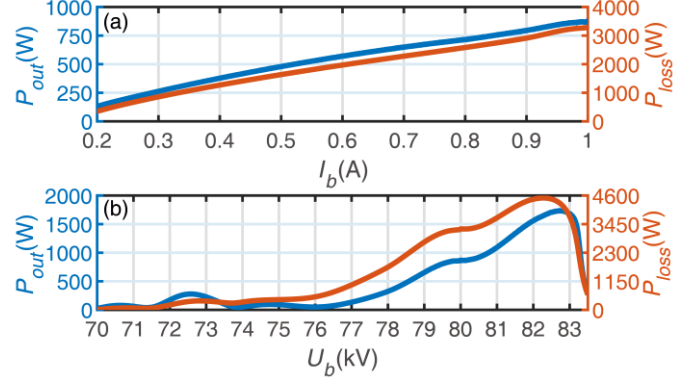

Fig. 7. Output and ohmic loss power in (a) current tuning and (b) voltage tuning.
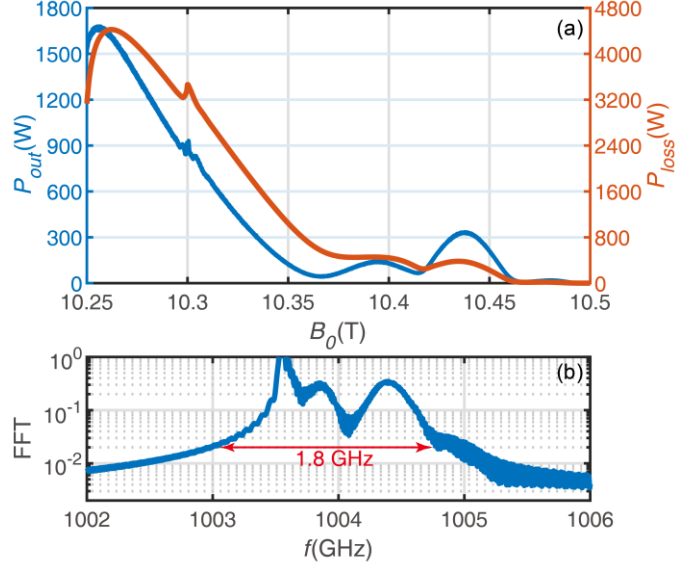

Fig. 8. Output and ohmic loss power in magnetic tuning.

10.3 – 10.5 T. The spectrum is calculated by the fast Fourier transform algorithm from the synthesis results of field amplitudes in 10.25 – 10.3 T and 10.3 – 10.5 T. At 10.25 T, the TE$_{4,8}$ mode is suppressed by the TE$_{3,6}$ mode. The peak power is 1.68 kW. The output frequency can cover 1.8 GHz (Fig. 8 (b)). The advantage of the synthesis method is that each tuning process can begin from a steady oscillation status to the hard-self-excitation region, and then to obtain the output characteristics. However, the synthesis method may cause the fluctuations in power curves at the point the curves intersected, for example the small peak at 10.3 T in Fig. 8. The fluctuation is induced by the change of the time derivations of the external magnetic field strength.

In the current, voltage, and magnetic tuning, the startup scenario is considered at 1 A, 80 kV, 10.3 T. The TE$_{4,8}$ mode is operated at the point because the I_{st} at 80 kV, 10.3 T is the lowest. It is easy to excite the operating mode. Normally, the operating point related to the highest beam-wave interaction efficiency is not the same as the startup point. In Fig. 8, the maximum of the beam-wave efficiency locates at a voltage higher than 80 kV, while in Fig. 9 the maximum of the beam-wave efficiency locates at a magnetic strength lower than
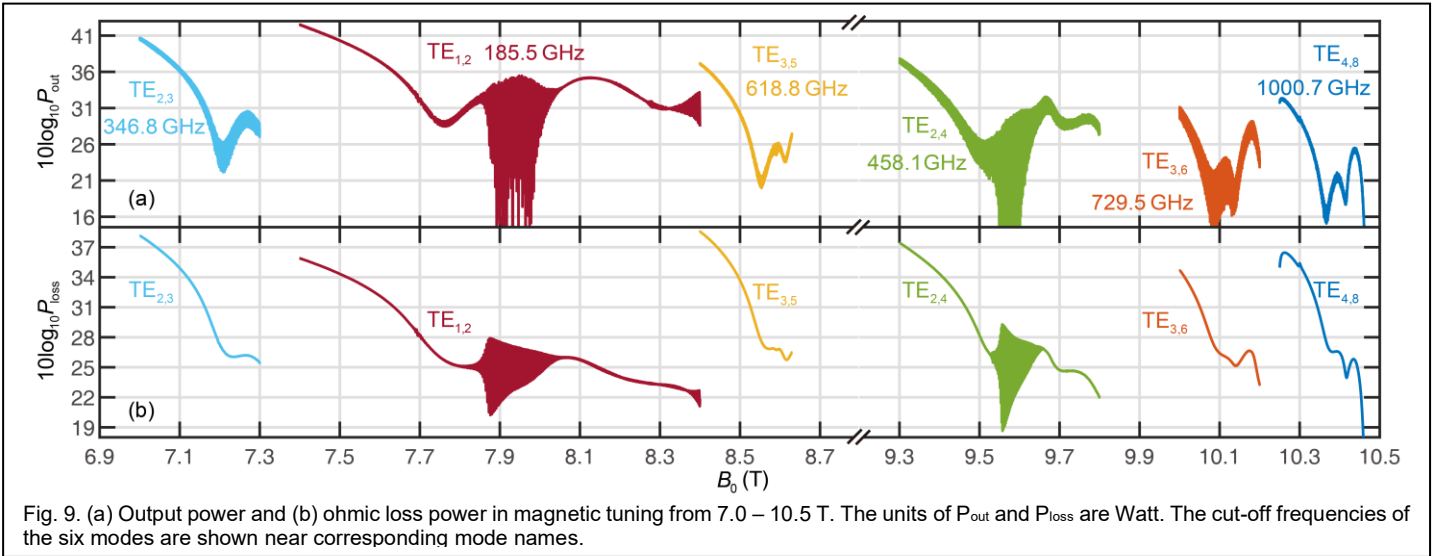
4

Fig. 9. (a) Output power and (b) ohmic loss power in magnetic tuning from 7.0 – 10.5 T. The units of P_{out} and P_{loss} are Watt. The cut-off frequencies of the six modes are shown near corresponding mode names.

10.3 T. The two cases are based on a similar mechanism. Based on the beam-wave synchronization equation (1), the increase of the operating voltage, and the decrease of the magnetic field strength will reduce the electron cyclotron frequency, which is related to the right-hand side of (1). The mismatch, called the detuning frequency, between the waveguide angular frequency and the electron cyclotron frequency is changed as well. The change of the detuning frequency means that the energy transfer process at high interaction efficiency point is longer than that at the startup point, which is similar as presented in [35].

B. Output Characteristics in Multi-Mode Step-Tuning

The output and ohmic loss power in multi-mode magnetic tuning are shown in Fig. 9. The output and ohmic loss power are calculated based on the time-domain multi-mode theory [30], [32]. The electron gun is modeled and simulated in MAGIC. The same model is simulated at nineteen linearly and equally spaced points between 7 T and 10.6 T (with a 0.2-T step size). Nineteen groups of beam parameters can be extracted from the nineteen groups of raw data. Parameters at other magnetic field strength are interpolated based on the nineteen groups of beam parameters with MATLAB. The interpolation algorithm is the piecewise cubic Hermite interpolating algorithm. The algorithm can ensure good accuracy as well as the continuity of interpolated functions.

In multi-mode step-tuning, the main operating mode ($TE_{4,8}$) and five parasitic modes ($TE_{1,2}$, $TE_{2,3}$, $TE_{2,4}$, $TE_{3,5}$, and $TE_{3,6}$) are considered as six candidate modes, which mean that each of them can be excited at a proper startup scenario. To verify this, the individual mode was simulated. To simplify the calculation, the calculation is divided into 6 parts. For every mode, only the potential competition modes are included. The correspondingly potential competition modes are determined based on the start-oscillation currents shown in Fig. 6. In the first part, the $TE_{2,3}$ mode is excited at 7.0 T. At 7.0 T, the output power is 11.69 kW, and the ohmic loss power is 6.49 kW. The parasitic modes are the $TE_{3,4}$ and $TE_{1,2}$ mode. The $TE_{2,3}$ mode is suppressed by the $TE_{1,2}$ mode at 7.3 T. In the second part, the $TE_{1,2}$ mode is excited at 7.4 T. At 7.4 T, the output power is 17.82 kW, and the ohmic loss power is 3.87 kW. The parasitic

modes are the $TE_{2,3}$ and $TE_{3,5}$ mode. Since the I_{st} of the $TE_{1,2}$ mode is lower than those of $TE_{2,3}$ and $TE_{3,5}$, the parasitic modes can hardly influence the $TE_{1,2}$ mode. The calculation is truncated at 8.4 T, although the $TE_{1,2}$ mode can still effectively interact with particles. In the third part, the $TE_{3,5}$ mode can be excited at 8.63 T, then the magnetic field strength is gradually tuned to 8.4 T. The parasitic mode is $TE_{1,2}$. At ~8.4 T, the output power is 5.15 kW, and the ohmic loss power is 2.39 kW. In the fourth part, the $TE_{2,4}$ mode can be excited at 9.3 T. At 9.3 T, the output power is 7.17 kW, and the ohmic loss power is 5.47 kW. In the fifth part, the $TE_{3,6}$ mode can be excited at 10.0 T. At 10.0 T, the output power is 1.30 kW, and the ohmic loss power is 2.88 kW. The sixth part about the $TE_{4,8}$ mode is demonstrated in the previous subsection.

IV. DISCUSSION

The misalignment among electron beams, interaction cavity, and confining magnet tends to be a key factor for gyrotron operating in high-harmonic conditions. In the hot experiment, the misalignment may source from many reasons, such as fabrication errors, poor assembly of the gyrotron, etc. [36]. The misalignment can be partly corrected by the careful designs of gyrotrons and the exquisite configuration of alignment systems. The misalignment affects the output performance by interfering with the beam-wave interaction efficiency, which means that the modes with high beam-wave coupling strength may have much resistance to the misalignment. Operating at 4th harmonic interaction requires tighter tolerance to the misalignment than the fundamental harmonic interaction. To address the misalignment correction and ease the challenges of operating directly at 4th harmonic in the experiment, a mode switching scheme was proposed in this paper. It allows to demostrate the gyrotron operationat fundamental mode, followed by 2nd and 3rd harmonic modes, and ended at the desired 4th harmonic mode.Ohmic loss is likely a critical factor worsening the performance of gyrotrons, especially in the high-frequency range [37]. The attenuation constant increases approximately linearly concerning the square root of operating frequency [37]. Besides, surface roughness and nonuniformity of main interaction cavities also have a relatively significant influence on gyrotron output

5

performance [26], [38].

V. CONCLUSION

The design of a 1-THz 4th-harmonic gyrotron, together with the development progress of this tube in Peking University, China, is presented in this paper. The interaction cavity is fully investigated and optimized. At 1 THz, the gyrotron has an output power of kW level with a relatively decent beam-wave interaction efficiency. The mode competition is carefully investigated and can be effectively suppressed. The cavity nonuniformity induced by the abrasion wear of cutting tools is investigated systematically. The several-micrometer difference in radius can increase the threshold of the start-oscillation current to 3 times higher. The main operation mode is the $TE_{4,8}$ mode. Based on the time-domain calculation, in magnetic tuning, the peak power can be up to 1.68 kW with an output efficiency of 2.1%, and the output frequency can cover ~1.8 GHz. The operating mode can be switched among 6 modes in the range of 7.0 – 10.5 T. Six modes can be excited sequentially in the range, i.e., $TE_{1,2}$ for fundamental harmonic, $TE_{2,3}$ and $TE_{2,4}$ for 2nd harmonic, $TE_{3,5}$ and $TE_{3,6}$ for 3rd harmonic, and $TE_{4,8}$ for 4th harmonic. The output power can be up to 17.82 kW ($TE_{1,2}$) in multi-mode switching. Based on the design scheme, the entire tube is under fabrication. The experiment is currently in preparation, and the measurement results will be reported in the near future.

REFERENCES

[1] P. H. Siegel, "Terahertz technology," *IEEE Trans. Microwave Theory Tech.,* vol. 50, no. 3, pp. 910-928, 2002. DOI: 10.1109/22.989974.

[2] E. A. Nanni, A. B. Barnes, R. G. Griffin, and R. J. Temkin, "THz Dynamic Nuclear Polarization NMR," *IEEE Trans Terahertz Sci Technol,* vol. 1, no. 1, pp. 145-163, 2011. DOI: 10.1109/TTHZ.2011.2159546.

[3] N. I. Chkhalo, N. N. Salashchenko, S. V. Golubev, D. Mansfeld, A. V. Vodopyanov, and L. Sjmaenok, "Source for extreme ultraviolet lithography based on plasma sustained by millimeter-wave gyrotron radiation," *Journal of Micro/Nanolithography,* vol. 11, no. 2, pp. 021123, 2012. DOI: 10.1117/1.JMM.11.2.021123.

[4] K. R. Chu, "The electron cyclotron maser," *Rev. Mod. Phys.,* vol. 76, no. 2, pp. 489-540, 2004. DOI: 10.1103/RevModPhys.76.489.

[5] G. S. Nusinovich, M. K. Thumm, and M. I. Petelin, "The gyrotron at 50: Historical overview," *J. Infrared Millim. Terahertz Waves,* vol. 35, no. 4, pp. 325-381, 2014. DOI: 10.1007/s10762-014-0050-7.

[6] J. H. IEEE Transactions on Electron DevicesBooske, R. J. Dobbs, C. D. Joye, C. L. Kory, G. R. Neil, G.-S. Park, J. Park, and R. J. Temkin, "Vacuum Electronic High Power Terahertz Sources," *IEEE Trans. THz Sci. Technol.,* vol. 1, no. 1, pp. 54-75, 2011. DOI: 10.1109/tthz.2011.2151610.

[7] M. Thumm, "State-of-the-Art of High-Power Gyro-Devices and Free Electron Masers," *J. Infrared Millim. Terahertz Waves,* vol. 41, no. 1, pp. 1-140, 2020. DOI: 10.1007/s10762-019-00631-y.

[8] V. Bratman, M. Glyavin, T. Idehara, Y. Kalynov, A. Luchinin, V. Manuilov, S. Mitsudo, I. Ogawa, T. Saito, Y. Tatematsu, and V. Zapevalov, "Review of Subterahertz and Terahertz Gyrodevices at IAP RAS and FIR FU," *IEEE Trans. Plasma Sci.,* vol. 37, no. 1, pp. 36-43, 2009. DOI: 10.1109/Tps.2008.2004787.

[9] A. N. Kuftin, M. D. Proyavin, M. V. Morozkin, E. M. Tai, S. Y. Kornishin, V. N. Manuilov, D. I. Sobolev, A. P. Fokin, A. I. Tsvetkov, G. G. Denisov, and M. Y. Glyavin, "Development and experimental tests of 250W/526 GHz/CW second harmonic gyrotron." pp. 1-2.

[10] I. V. Bandurkin, A. P. Fokin, M. Y. Glyavin, A. G. Luchinin, I. V. Osharin, and A. V. Savilov, "Demonstration of a Selective Oversized Cavity in a Terahertz Second-Harmonic Gyrotron," *IEEE*

[11] *Electron Device Lett.,* vol. 41, no. 9, pp. 1412-1415, 2020. DOI: 10.1109/LED.2020.3010445.

S. Spira-Hakkarainen, K. E. Kreischer, and R. J. Temkin, "Submillimeter-wave harmonic gyrotron experiment," *IEEE Trans. Plasma Sci.,* vol. 18, no. 3, pp. 334-342, 1990. DOI: 10.1109/27.55903.

[12] X. Guan, W. Fu, and Y. Yan, "A 0.4-THz Second Harmonic Gyrotron with Quasi-Optical Confocal Cavity," *J. Infrared Millim. Terahertz Waves,* vol. 38, no. 12, pp. 1457-1470, 2017. DOI: 10.1007/s10762-017-0432-8.

[13] Z. Wang, and S. Yu, "The Nonlinear Design and Experiment of a 0.68-THz Second Harmonic Gyrotron," *IEEE Trans. Plasma Sci.,* vol. 48, no. 8, pp. 2952-2957, 2020. DOI: 10.1109/TPS.2020.3004559.

[14] A. Q. Zhao, and B. S. Yu, "The Nonlinear Designs and Experiments on a 0.42-THz Second Harmonic Gyrotron With Complex Cavity," *IEEE Trans. Electron Devices,* vol. 64, no. 2, pp. 564-570, 2017. DOI: 10.1109/TED.2016.2642984.

[15] W. Fu, X. Guan, C. Chen, X. Li, X. Yuan, and Y. Yan, "Design and Experiment of a 220/420-GHz Gyrotron for Nondestructive Evaluation," *IEEE Trans. Electron Devices,* vol. 61, no. 7, pp. 2531-2537, 2014. DOI: 10.1109/TED.2014.2322083.

[16] T. Idehara, and S. P. Sabchevski, "Development and Applications of High—Frequency Gyrotrons in FIR FU Covering the sub-THz to THz Range," *J. Infrared Millim. Terahertz Waves,* vol. 33, no. 7, pp. 667-694, 2012. DOI: 10.1007/s10762-011-9862-x.

[17] T. Idehara, H. Tsuchiya, O. Watanabe, L. Agusu, and S. Mitsudo, "The first experiment of a THz gyrotron with a pulse magnet," *Int. J. Infrared Millim. Waves,* vol. 27, no. 3, pp. 319-331, 2006. DOI: 10.1007/s10762-006-9084-9.

[18] T. Idehara, T. Saito, H. Mori, H. Tsuchiya, L. Agusu, and S. Mitsudo, "Long Pulse Operation of the THz Gyrotron with a Pulse Magnet," *Int. J. Infrared Millim. Waves,* vol. 29, no. 2, pp. 131-141, 2008. DOI: 10.1007/s10762-007-9312-y.

[19] V. Bratman, Y. K. Kalynov, and V. Manuilov, "Large-orbit gyrotron operation in the terahertz frequency range," *Phys. Rev. Lett.,* vol. 102, no. 24, pp. 245101, 2009. DOI: 10.1103/PhysRevLett.102.245101.

[20] T. Idehara, I. Ogawa, S. Mitsudo, Y. Iwata, S. Watanabe, Y. Itakura, K. Ohashi, H. Kobayashi, T. Yokoyama, V. E. Zapevalov, M. Y. Glyavin, A. N. Kuftin, O. V. Malygin, and S. P. Sabchevski, "A high harmonic gyrotron with an axis-encircling electron beam and a permanent magnet," *IEEE Trans. Plasma Sci.,* vol. 32, no. 3, pp. 903-909, 2004. DOI: 10.1109/TPS.2004.827614.

[21] F.-H. Li, C.-H. Du, Z.-W. Zhang, S.-Q. Li, Z.-C. Gao, J.-F. Zhu, G.-W. Ma, Q.-L. Huang, H.-G. Ma, and L. Zhang, "Development of a magnetic cusp gun for a 1-THz harmonic gyrotron," *IEEE Trans. Electron Devices*, 2021. DOI: 10.1109/TED.2021.3120699.

[22] Y. Y. Lau, "Effects of cathode surface roughness on the quality of electron beams," *J. Appl. Phys.,* vol. 61, no. 1, pp. 36-44, 1987. DOI: 10.1063/1.338833.

[23] A. V. Gaponov, V. A. Flyagin, A. L. Gol'Denberg, G. S. Nusinovich, S. E. Tsimring, V. G. Usov, and S. N. Vlasov, "Powerful millimetre-wave gyrotrons," *Int. J. Electron.,* vol. 51, no. 4, pp. 277-302, 1981. DOI: 10.1080/00207218108901338.

[24] C. Yuan, T. Chang, N. Chen, and Y. Yeh, "Magnetron injection gun for a broadband gyrotron backward-wave oscillator," *Phys. Plasmas,* vol. 16, no. 7, pp. 073109, 2009. DOI: 10.1063/1.3187903.

[25] L. Zhang, W. He, C. R. Donaldson, and A. W. Cross, "Investigation on the optimal magnetic field of a cusp electron gun for a W-band gyro-TWA," *Phys. Plasmas,* vol. 25, no. 5, pp. 053104, 2018. DOI: 10.1063/1.5027070.

[26] M. P. Kirley, and J. H. Booske, "Terahertz Conductivity of Copper Surfaces," *IEEE Trans. THz Sci. Technol.,* vol. 5, no. 6, pp. 1012-1020, 2015. DOI: 10.1109/TTHZ.2015.2468074.

[27] E. Hammerstad, and O. Jensen, "Accurate models for microstrip computer-aided design." pp. 407-409.

[28] K. R. Chu, H.-Y. Chen, C.-L. Hung, T.-H. Chang, L. R. Barnett, S.-H. Chen, T.-T. Yang, and D. J. Dialetis, "Theory and experiment of ultrahigh-gain gyrotron traveling wave amplifier," *IEEE Trans. Plasma Sci.,* vol. 27, no. 2, pp. 391-404, 1999. DOI: 10.1109/27.772266.

[29] Y. J. Huang, K. R. Chu, and M. Thumm, "Self-consistent modeling of terahertz waveguide and cavity with frequency-dependent

conductivity," *Phys. Plasmas,* vol. 22, no. 1, pp. 013108, 2015. DOI: 10.1063/1.4905627.

[30]   C.-H. Du, and P.-K. Liu, "Nonlinear full-wave-interaction analysis of a gyrotron-traveling-wave-tube amplifier based on a lossy dielectric-lined circuit," *Phys. Plasmas,* vol. 17, no. 3, pp. 033104, 2010. DOI: 10.1063/1.3339935.

[31]   X.-B. Qi, C.-H. Du, and P.-K. Liu, "High-Efficiency Excitation of a Third-Harmonic Gyrotron," *IEEE Trans. Electron Devices,* vol. 62, no. 10, pp. 3399-3405, 2015. DOI: 10.1109/ted.2015.2461657.

[32]   Z.-C. Gao, C.-H. Du, F.-H. Li, S. Pan, Z.-W. Zhang, and P.-K. Liu, "Strong Dispersive Propagation of Terahertz Wave: Time-Domain Self-Consistent Modeling of Metallic Wall Losses," *Advanced Theory and Simulations,* vol. 3, no. 3, pp. 1900218, 2020. DOI: 10.1002/adts.201900218.

[33]   C.-H. Du, X.-B. Qi, L.-B. Kong, P.-K. Liu, Z.-D. Li, S.-X. Xu, Z.-H. Geng, and L. Xiao, "Broadband Tunable Pre-Bunched Electron Cyclotron Maser for Terahertz Application," *IEEE Trans. THz Sci. Technol.,* vol. 5, no. 2, pp. 236-243, 2015. DOI: 10.1109/tthz.2014.2378071.

[34]   G. S. Nusinovich, A. N. Vlasov, and T. M. Antonsen, "Nonstationary Phenomena in Tapered Gyro-Backward-Wave Oscillators," *Phys. Rev. Lett.,* vol. 87, no. 21, 2001. DOI: 10.1103/physrevlett.87.218301.

[35]   Z.-C. Gao, C.-H. Du, F.-H. Li, and P.-K. Liu, "Terahertz gyrotrons with inhomogeneous magnetic fields to suppress mode competition and enhance efficiency," *J. Appl. Phys.,* vol. 129, no. 4, pp. 043306, 2021. DOI: 10.1063/5.0032597.

[36]   Z. C. Ioannidis, K. A. Avramidis, G. Gantenbein, S. Illy, T. Kobarg, I. G. Pagonakis, T. Rzesnicki, and J. Jelonnek, "Development and Experimental Verification of an XY-Table for the Optimization of the Alignment of High-Power Gyrotrons," *IEEE Trans. Electron Devices,* vol. 66, no. 4, pp. 1954-1959, 2019. DOI: 10.1109/TED.2019.2899163.

[37]   S. Kao, C. Chiu, and K. Chu, "A study of sub-terahertz and terahertz gyrotron oscillators," *Phys. Plasmas,* vol. 19, no. 2, pp. 023112, 2012. DOI: 10.1063/1.3684663.

[38]   K. Lomakin, G. Gold, and K. Helmreich, "Analytical Waveguide Model Precisely Predicting Loss and Delay Including Surface Roughness," *IEEE Trans. Microwave Theory Tech.,* vol. 66, no. 6, pp. 2649-2662, 2018. DOI: 10.1109/TMTT.2018.2827383.